

Aerodynamic Shape Optimization of a Blended-Wing-Body Regional Transport for a Short Range Mission

Thomas A. Reist* and David W. Zingg†

*Institute for Aerospace Studies, University of Toronto
4925 Dufferin St., Toronto, Ontario, M3H 5T6, Canada*

The blended-wing-body represents a potential revolution in efficient aircraft design. A lift-constrained drag-minimization optimization problem is solved for the optimal shape of a blended-wing-body transonic regional jet. A Newton-Krylov solver for the Euler and Reynolds-Averaged Navier-Stokes (RANS) equations is coupled with a gradient-based optimizer, where gradients are calculated via the discrete adjoint method. A 98-passenger regional jet is optimized for a 500nmi mission at 40,000ft and Mach 0.8. A series of single and multipoint optimization problems using both the Euler and RANS equations are considered in order to examine the trade-offs between the imposition of different constraints including trim and longitudinal static stability. Drag reductions of up to 55% and 38% are achieved for the Euler and RANS-based optimizations respectively. In each case an elliptical lift distribution is attained on the wing, shocks are eliminated, and in the RANS-based optimization the large regions of highly separated flow on the baseline design are greatly reduced. These drag reductions are achieved while both trimming and stabilizing the baseline design.

Nomenclature

x, y, z	Stream-wise, span-wise and vertical coordinates
b	Total aircraft semi-span
c	Local chord length
c_{root}	Chord length at the aircraft center-line
MAC	Mean aerodynamic chord
S	Reference planform area
t/c	Section thickness normalized with local chord length
C_L, C_D, C_M	Lift, drag and pitching moment coefficients of the entire aircraft
AoA	Angle-of-attack
M	Freestream Mach number
q_∞	Freestream dynamic pressure
a	Sound speed at cruise conditions
W	Aircraft weight
MTOW	Maximum take-off weight
OEW	Operating empty weight
c_T	Thrust specific fuel consumption
K_n	Static margin as percent of the MAC
Δ_{CG}	Center of gravity perturbation design variable

*Ph.D. Candidate, AIAA Student member, tom.reist@utoronto.ca

†Professor and Director, Canada Research Chair in Computational Aerodynamics and Environmentally Friendly Aircraft Design, J. Armand Bombardier Foundation Chair in Aerospace Flight, Associate Fellow AIAA, dwz@oddjob.utias.utoronto.ca

I. Introduction

WITH increasing oil prices and concern about both the exhaustion of fossil fuels and their contribution to climate change, the need for more fuel efficient aircraft is becoming more pronounced for both economic and environmental reasons. Although there have been great advances in transport aircraft efficiency since the introduction of the de Havilland Comet in 1952, the conventional tube-wing configuration remains to this day. Performance improvements have come from modifications to aerodynamic design, such as the use of winglets and supercritical airfoils, as well as high performance materials and increasingly fuel efficient engines. However a step change in fuel efficiency may be realized through novel configurations. One such configuration that has received much attention in recent years is the blended-wing-body (BWB). This design combines the aircraft fuselage and wings into one tightly integrated airframe with improved aerodynamic, structural, propulsive, and acoustic efficiency.

The BWB has the potential to be more aerodynamically efficient than conventional configurations for several reasons. For a given internal volume, the BWB has less wetted surface area, leading to a better lift-to-drag ratio.¹ It has also been shown to be more area-ruled than conventional designs, which allows for reduced wave drag and potentially higher cruise speeds.¹ The overall shape of the BWB is also cleaner than a conventional design, leading to reduced interference drag. Structurally, the aerodynamic lifting loads are more closely aligned with the weight of the aircraft due to the lifting fuselage, leading to reduced bending loads in the main wing structure and therefore lower structural weight.¹ The use of a well integrated propulsion system, such as boundary-layer-ingestion or distributed propulsion, can lead to propulsive efficiencies. A well integrated propulsion system on the top of the aircraft can also provide significant noise reductions due to the acoustic shielding provided by the aerodynamic surfaces.² The highly integrated nature of the design allows for efficiency improvements; however this also increases the design challenges stemming from such a highly coupled configuration.

One of the main structural challenges associated with the BWB is the lack of the efficient cylindrical pressure vessel present in conventional designs. Much work has been dedicated to the design of efficient composite structures tailored for handling these pressure loads.³⁻⁵ Due to its tailless nature, stability and control can be challenging with this design. Work has been done on addressing some of these issues.^{6,7} With such a radically different design, certification and customer acceptance must also be addressed. Finally, perhaps the biggest obstacle to the development of the BWB is the financial risk associated with pursuing such a novel design. However, as rising fuel prices continue to reduce operating profits, the potential benefits of this unconventional design may justify its development.

Several large projects around the world have focused on the development of the BWB design. In the United States, Boeing and NASA have been involved in the identification and development of enabling technologies required for the BWB design,^{1,3,6,8-10} with contributions leading to the X-48 flight demonstrators. A BWB design focused on noise reduction has been developed as part of Cambridge and MIT's 'Silent' Aircraft Initiative.^{2,11} In Europe, two of the main projects relating to BWB design are the Multidisciplinary Optimization of a Blended Wing Body (MOB)¹² and the Very Efficient Large Aircraft (VELA)¹³ projects.

Aerodynamic shape optimization (ASO) has been applied to the BWB design at a variety of fidelity levels. Peigin and Epstein¹⁴ used a Navier-Stokes solver and genetic optimizer for the optimization of the MOB configuration for multiple operating points with airfoil, dihedral and twist design variables. Qin et al.¹⁵ performed spanload optimization through twist modification as well as 3D surface optimization using both Euler and Navier-Stokes solvers. Both airfoil and sweep optimization were performed by Le Moigne and Qin¹⁶ using a discrete adjoint method with an Euler solver. They demonstrated that the imposition of pitching moment constraints has a large impact on the optimal shape yet only a small performance penalty must be paid. The performance improvements obtained using Euler-based optimization are also realized when evaluated with a Navier-Stokes solver. A small BWB was optimized by Kuntawala et al.¹⁷ using a large number of geometric design variables for full 3D surface optimization.

Historically, the focus of BWB design investigations has been on large capacity aircraft in the 400-1000 passenger range. The BWB's intrinsic design features lend themselves well to large aircraft. However this design may also offer advantages in the regional jet segment. Nickol examined a series of BWB aircraft ranging from 98-400 passengers.⁹ As expected, the fuel burn benefit was most significant for the larger aircraft, with the 98 passenger aircraft burning more fuel than a comparable tube-wing aircraft. However, the fuel burn disadvantage of the small BWB was highly sensitive to drag. Thus, if a suitable drag reduction can be achieved through aerodynamic shape optimization, the BWB could potentially be more fuel efficient than the tube-wing aircraft for a variety of aircraft classes.

II. Optimization Methodology

The aerodynamic shape optimization algorithm used comprises three main components: 1) a multiblock Newton-Krylov solver for the Euler and Reynolds-Averaged Navier-Stokes (RANS) equations, 2) a B-spline geometry parameterization which is coupled with a linear elasticity mesh movement strategy, and 3) the gradient-based optimizer SNOPT with gradients calculated using the discrete adjoint method.

The flow solver is a multiblock finite-difference solver which uses summation-by-parts operators for spatial discretization and simultaneous approximation terms for the imposition of boundary conditions and block interface conditions. The Krylov subspace method Generalized Minimum Residual (GMRES) is used with approximate Schur preconditioning for the solution of the discrete equations. The one-equation Spalart-Allmaras turbulence model is used for the modeling of turbulent flows. Details of the flow solver can be found in Hicken and Zingg¹⁸ and Osusky and Zingg.¹⁹

At each optimization iteration for which a geometric shape change occurs, the computational grid must be moved to reflect this change. To accomplish this, each block of the computational grid is fitted with a B-spline volume. As the B-spline control points on the aerodynamic surface are moved by the optimizer, each B-spline volume block is treated as a linear elastic solid, for which a finite-element solution is obtained to define the new shape of the B-spline volume. The computational grid is then recovered from this new B-spline volume. This method has been found to be very robust for large shape changes while being computationally inexpensive. Details can be found in Hicken and Zingg.²⁰

Due to the high cost of evaluating the flow equations, a gradient-based optimizer is used for optimization, as gradient-based optimizers typically require fewer function evaluations than genetic algorithms.²¹ The penalty paid is that for multimodal optimization problems only a local optimum may be found. This can be addressed using the gradient-based global optimization techniques proposed by Chernukhin and Zingg.²² The gradients of the objective and constraints are evaluated using the discrete adjoint method. This method is advantageous for problems with many design variables, as the cost of the gradient evaluation is nearly independent of the number of design variables. The gradient-based optimizer SNOPT is used, as it allows for the solution of large-scale constrained problems. Details of the adjoint method and its integration with the flow solver and mesh movement are given by Hicken and Zingg²⁰ while the details of SNOPT are described by Gill et al.²³

The above algorithm has been used extensively for ASO of various wing geometries including induced drag minimization of non-planar wings,²⁴ optimization of wings in turbulent flows,²⁵ the investigation of the multimodality of ASO problems²² and the optimization of BWB aircraft.¹⁷

III. Baseline Design

The aircraft considered in this work is intended to serve as a regional jet with a single-class capacity of approximately 100 passengers and four crew, while having a maximum range capability of 2000nmi with 100nmi reserves. The first step in generating a geometric shape is to size the cabin such that it fits all passengers, crew, aisles and monuments (such as lavatories and galleys) so as to produce a shape that can be well integrated into the rest of the airframe in order to avoid unnecessary structural weight, while at the same time providing a pressure vessel shape that is as efficient as possible. As in many BWB concepts^{1,2,9,26} a ‘home plate’ shaped cabin is utilized. The length of the outboard cabin wall is defined via the required cabin height (plus an allowance for structure space), and the airfoil thickness at the corresponding spanwise location. The width of the cabin is increased by adding seats until the required number of seats, aisles and monuments are accommodated. Appropriately sized cargo holds are added outboard of the passenger compartment. The remainder of the airframe is designed around this cabin via an iterative procedure, with the aim of avoiding unnecessary surface area and excessive structural weight. The weight at each shape iteration is calculated as described below. The baseline design is shown in Figure 1.

For a given aircraft shape a weight estimate is required. The weight of the center body structure is obtained using the method of Bradley.²⁶ The remaining structure, system, fuel and operational item weights are assumed to be similar to those for conventional tube-wing aircraft and are obtained using the relations of Roskam.²⁷ All weight estimates are based on current technology levels. This weight estimation methodology has been evaluated for a series of BWB sizes and agrees well with the results of Nickol.^{9a} A summary of

^aAdvanced technology factors similar to those used by Nickol are included when evaluating weights for comparison with his results.

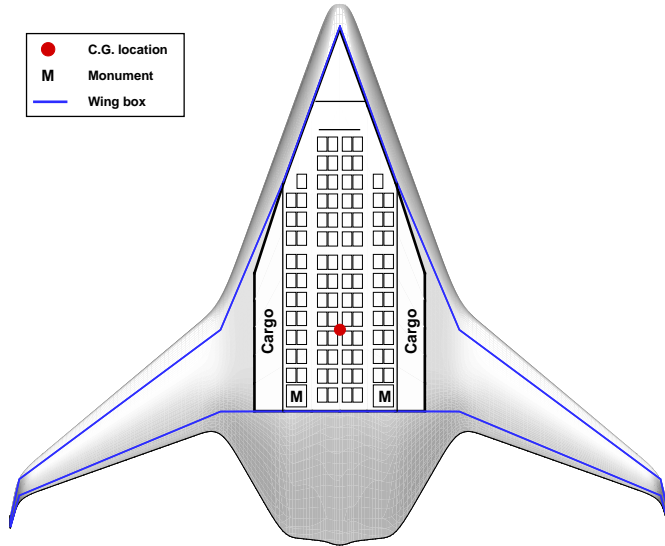


Figure 1: Baseline design with passenger layout and wingbox structure.

Capacity

Passengers	98
Crew	4
Cabin floor area	593 ft ²
Cargo volume	685 ft ³

Geometry

Planform area	2177 ft ²
Total span	90 ft
Length	74 ft
MAC	44 ft
Aspect ratio	3.7

Weight

MTOW	96,760 lb
OEW	54,710 lb
Payload	23,380 lb
Wing load at MTOW	44 lb/ft ²

Cruise conditions

Design range	500 nmi
Altitude	40,000 ft
Reynolds number*	70×10^6
Mach number	0.80
x_{CG}/c_{root}	0.65

* Based on full aircraft MAC.

Table 1: Baseline design summary.

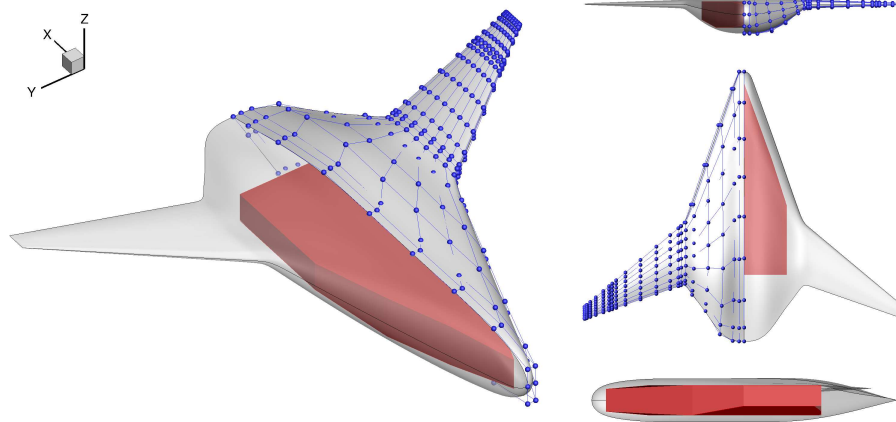


Figure 2: Baseline geometry with cabin shape. Blue spheres are the surface B-spline control points used to define the geometry. The red polyhedron is the cabin shape.

the aircraft design is shown in Table 1. While winglets are shown on the conceptual design, they are not included in the optimization studies presented herein.

As shown by Mozdzanowska and Hansman,²⁸ most regional jets are not flown at their maximum range for most missions. Thus, optimization is performed for a single stage 500nmi flight with 100nmi reserves at Mach 0.80 and 40,000ft, details of which are included in Table 1. The chosen cruise altitude of 40,000ft is higher than would be used by a tube-wing design for a similar mission, since, as demonstrated by Martínez-Val et al.,²⁹ the low wing loading of the BWB design causes it to attain optimum cruise efficiency at a higher altitude than tube-wing designs. While such a high cruise altitude for a short range mission would have air traffic management and structural implications, these are not considered here.

The baseline geometry, along with its B-spline parameterization, and the cabin shape are shown in Figure 2. The cabin shape generated via the method described above forms the red internal polyhedron.

	Lower bound	Variable/Constraint	Upper bound
	Body design variables		
Geometric Design Variables (Total 332)	$0.2c_{\text{root}}$	Chord	$1.0c_{\text{root}}$
	0.01	Taper	0.50
	-30.0°	Twist	$+30.0^\circ$
	$-0.10(t/c)_{\text{orig}}$	6 airfoil sections*	$+0.10(t/c)_{\text{orig}}$
	Wing design variables		
	0.0°	Leading-edge sweep	45.0°
Geometric Constraints	$0.02c_{\text{root}}$	Chord	$0.30c_{\text{root}}$
	0.10	Taper	0.25
	-10.0°	Twist (linear)	$+10.0^\circ$
	$-0.05(t/c)_{\text{orig}}$	12 airfoil sections*	$+0.05(t/c)_{\text{orig}}$
	$0.59c_{\text{root}}$	Total semi-span	$0.59c_{\text{root}}$
	$0.39c_{\text{root}}^2$	Reference area	$0.39c_{\text{root}}^2$
	–	Cabin shape	–

* The upper and lower bounds represent the amount, in t/c , by which the B-spline control points controlling the airfoil sections can move from their initial distance from the chordline. Separate thickness constraints are imposed to ensure minimum/maximum thickness requirements are maintained.

Table 2: Geometric design variables and constraints common to each optimization problem.

This polyhedron forms a constraint for the optimizer which prevents the aerodynamic surface from entering the cabin. The baseline airfoils on the body are selected to be no more than 17% thick and to adequately house the cabin, with little consideration given to aerodynamic performance. Thus the baseline design is not expected to be efficient. The airfoils on the wing are slightly modified versions of the NASA SC(2)-0414 supercritical airfoil.

IV. Aerodynamic Shape Optimization

A series of optimization cases are considered, each examining the effect of various design variables, constraints, and flow models. Each optimization case has the same geometric freedom, which is detailed in Table 2, and the objective is to minimize drag. The reference area and span are constrained due to the absence of structural modeling in the optimization. No volume constraints are used; instead changes in wing thickness are restricted. The limits have been set to ensure that adequate structural depth and fuel capacity are maintained. The cabin constraint ensures that the cabin, shown by the red polyhedron in Figure 2, is not violated by the aerodynamic surface during the optimization. Four optimization problems are considered, each with a different set of variables and constraints as detailed in Table 3. The first four cases in Table 3 use the Euler equations, which are solved on 24 block, 950,000 node grids. The last Euler optimization problem involves multiple operating points and is described in Subsection B. The Euler-based Case C_M is repeated using the RANS equations which are solved on a 120 block, 5.6×10^6 node grids with an average off-wall spacing of 4×10^{-7} MAC ($y^+ = 0.9$).

A. Trim and Stability Constraint Implementation

Consideration of trim and stability during optimization is much more crucial when optimizing a full flying wing configuration than when optimizing a wing in isolation, as the trim and stability of the aircraft must be achieved solely by the lifting surface(s) which are being optimized. In this work, trim and longitudinal static stability are considered. The two conditions for trim are given by

$$C_L = \frac{W}{q_\infty S} \quad \text{and} \quad C_M = 0 \quad (1)$$

Flow	Case	Design variables		Constraints		
		AoA	Δ_{CG}	C_L	C_M	K_n
Euler	C_M	$\pm 3.00^\circ$	–	0.219	0.00	–
	C_M/K_n	$\pm 3.00^\circ$	–	0.219	0.00	5.0%
	$C_M/K_n - CG$	$\pm 3.00^\circ$	$\pm 0.05c_{root}$	0.219	0.00	5.0%
	MP C_M	$\pm 3.00^\circ$	–	0.219*	0.00†	–
RANS	C_M	$\pm 3.00^\circ$	–	0.219	0.00	–

* This C_L target corresponds to the center quadrature point.

† The trim constraint is enforced only at the center quadrature point where $C_L = 0.219$ and $M = 0.80$.

Table 3: Additional design variable and constraints for each optimization case with design variable bounds.

where W is the weight of the aircraft, q_∞ is the freestream dynamic pressure, and S is the reference planform area. The two conditions for natural longitudinal static stability are

$$C_M = 0 \quad \text{for some} \quad C_L > 0 \quad (2)$$

and

$$K_n = \frac{x_{NP} - x_{CG}}{MAC} = -\frac{\partial C_M}{\partial C_L} > 0 \quad (3)$$

where K_n is the static margin, and x_{NP} and x_{CG} are the locations of the aircraft neutral point and center of gravity, respectively. The computation of the trim conditions is straightforward and obtaining their gradients requires the solution of two adjoint problems, one for C_L and one for C_M . The static margin constraint, $K_n = -\frac{\partial C_M}{\partial C_L} > 0$, is calculated by performing an additional flow solve at the design point with a perturbed angle-of-attack. This allows the construction of a first-order accurate finite-difference approximation for $\frac{\partial C_M}{\partial C_L}$. Thus, the static margin constraint requires an additional flow solve and two additional adjoint solutions to obtain its gradient. To reduce the computation time, the flow solution at the perturbed state is warmstarted from the flow solution at the base state. Similarly, the Krylov solver used for the solution of the flow adjoint equations uses the adjoint vector from the base point as the initial guess for the adjoint solutions at the perturbed state. These warmstarting methods have shown to have very little impact on the optimizer convergence behaviour and can reduce the computational expense of the static margin constraint by up to 40%.

Because the pitching moment and static margin are linearly dependent on the location of the center of gravity (CG), a method of correlating geometric changes with CG movement is required. For this, a series of low-fidelity relations are used such that the CG location moves with the geometry (e.g. as the wing sweep increases, the CG moves aft due to the movement of the wing structure and fuel weights) and also scales with the geometry (e.g. the wing structural weight scales with wing sweep, span, area and thickness) based on the same low-fidelity relations used to obtain the initial weight estimate described in Section III. Note that the structural weight does not scale with changes in aerodynamic loading (e.g. if lift is shifted to the outboard portion of the wing, and hence higher bending loads in the wing structure are generated, no structural weight increase results.) Due to the low-fidelity nature of this model and the preliminary nature of the design problem, an additional design variable, Δ_{CG} , is introduced which allows the CG to be moved about the point calculated by the weight model, i.e.

$$x_{CG} = x_{CG_{calc}} + \Delta_{CG} \quad (4)$$

Note that this design variable is only active in certain cases which have a static margin constraint. Optimization cases with only a trim constraint would move the CG to its aft limit in order to maintain aft-loaded sections; however if the static margin constraint is active, a CG location which is a compromise between the trim and stability constraints is chosen by the optimizer. Without this freedom in the CG location, the center of pressure and neutral point are effectively defined by the trim and static margin constraints respectively, and once planform changes aimed at moving the neutral point are exhausted due to limits on geometric flexibility, the optimizer is forced to contort the pressure distributions through section changes so as to properly place both the center of pressure and neutral point, as will be discussed later.

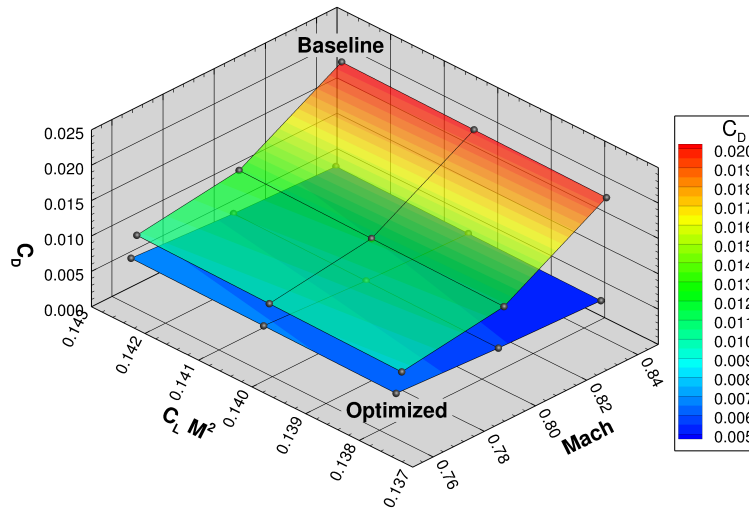


Figure 3: Drag coefficient for a series of aircraft weights and cruise speeds. Each node is a quadrature point used in the multipoint optimization. Performance of the baseline and multipoint optimized designs are shown by the two surfaces.

B. Multipoint Optimization

In order to ensure good off-design performance, a multipoint optimization problem is considered which uses the weighted integral approach of Buckley and Zingg.³⁰ Instead of minimizing drag at a single operating point, the objective to be minimized, J , is the weighted integral of drag over a range of aircraft weights and cruise speeds. This is expressed as

$$\begin{aligned}
 J &= \sum_{i=1}^{N_W} \sum_{j=1}^{N_M} \omega_{i,j} \Psi(W_i, M_j) C_D(W_i, M_j) \\
 &\approx \int_M \int_W \Psi(W, M) C_D(W, M) dW dM
 \end{aligned} \tag{5}$$

where Ψ is a user-defined weighting function which assigns a higher priority to certain cruise speeds and aircraft weights, N_W and N_M are the number of aircraft weight and cruise Mach number quadrature points respectively, and $\omega_{i,j}$ are the quadrature weights used to approximate the integral. Figure 3 shows C_D with respect to aircraft weight and cruise speed for the baseline and multipoint optimized designs. The volume under these surfaces is the objective expressed in Eqn. 5, with the spheres being the locations of the quadrature points in the $W - M$ plane.

For this work the multipoint optimization case, denoted Case MP C_M , uses three quadrature points in each of the weight and Mach number dimensions for a total of nine quadrature points. The three Mach number quadrature points correspond to three different cruise speeds of Mach 0.76, 0.80, and 0.84. For each of these possible missions the aircraft weight at the start, middle, and end of cruise form the three weight dimension quadrature points. No user-defined weighting function is used ($\Psi = 1$) and the quadrature weights $\omega_{i,j}$ correspond to the trapezoidal rule. The middle quadrature point (Mach 0.8 at the midpoint of cruise) is at the same conditions as Case C_M . A trim constraint is applied at this quadrature point only, as the absence of a trim-effector model does not allow the design to be trimmed at other operating points.

V. Design Performance

This section presents the performance of each optimized design. All of the Euler analyses are performed on refined grids of 1.6×10^6 nodes, and the RANS analyses are performed on 10.0×10^6 node grids with an average off-wall spacing of 3.5×10^{-7} MAC ($y^+ = 0.7$). The refined grids are the reason for the angles-of-attack and some of the constraints not falling exactly within their bounds, which are satisfied during the optimizations.

Case	AoA	C_L	C_M	K_n	L/D
Baseline	1.85°	0.219	-0.0211	-2.8%	18.3
C_M	3.01°	0.219	0.0000	-1.2%	40.4
C_M/K_n	3.02°	0.219	0.0002	+4.9%	38.3
C_M/K_n -CG	3.01°	0.219	0.0001	+4.9%	39.6
MP C_M^*	2.28°	0.219	0.0000	-2.1%	40.0

* Performance at the center quadrature point ($M = 0.80$, $C_L = 0.219$).

Table 4: Summary of performance for the baseline and Euler-optimized cases.

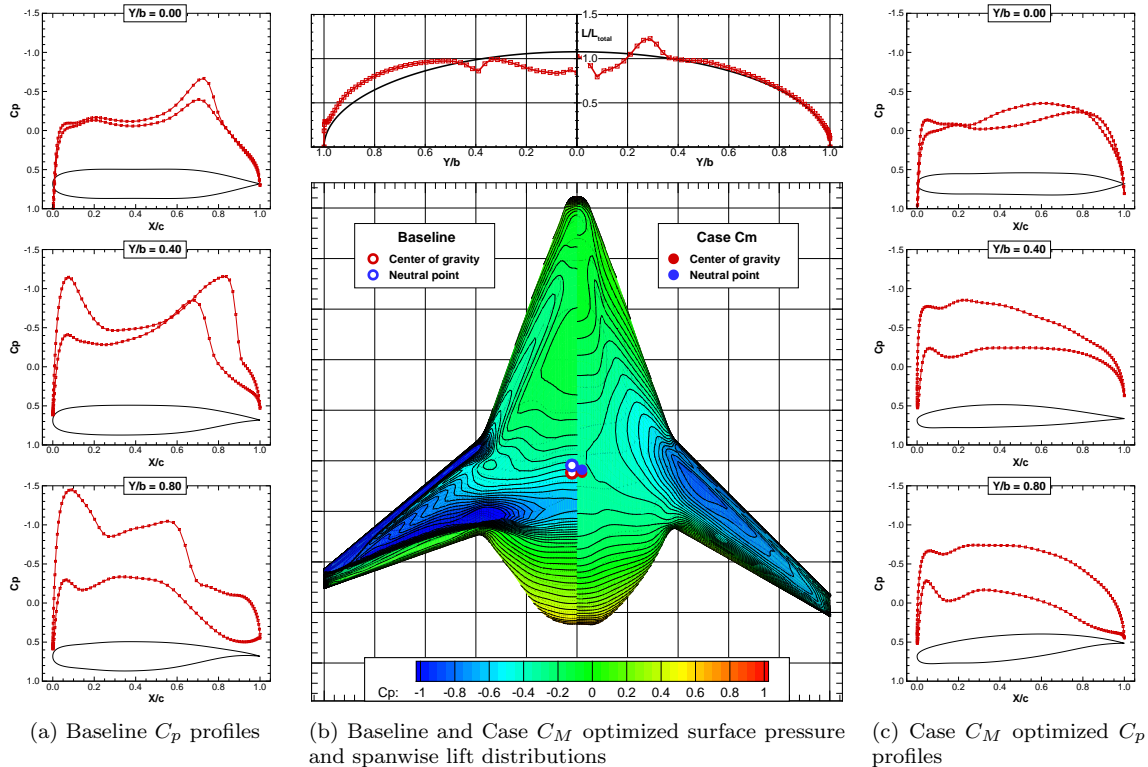


Figure 4: Inviscid pressure and spanwise lift distributions on the baseline and Case C_M optimized designs.

A. Euler-Based Optimization Results

A summary of the performance of each Euler-optimized design as well as the baseline is shown in Table 4. The pressure distribution on the baseline design is shown in the left half of Figure 4. A strong shock is present over most of the upper surface and the spanwise lift distribution is non-elliptical. The result of minimizing the sum of wave and induced drag subject to lift and pitching moment constraints is shown in Case C_M in the right half of Figure 4. A 55% drag reduction is achieved by eliminating the shock – and hence wave drag – and by achieving a spanwise lift distribution which is close to elliptical on the wing. Note however that the CG is aft of the neutral point, and thus this design is unstable.

The result of imposing the 5% static margin constraint is shown in the left side of Figure 5 for Case C_M/K_n . A 5.5% drag penalty is incurred relative to Case C_M as a result of the static margin constraint. As in Case C_M , the elliptical distribution is recovered on the wing, and the shock on most of the aircraft is eliminated, with the exception of a small localized shock at 80% span. Since the CG is relatively static^b and

^bThe CG moves with the geometry as described in Section A. However, most of the aircraft weight is located in the body which has a relatively static local CG, thus the calculated CG location changes very little during the optimization.

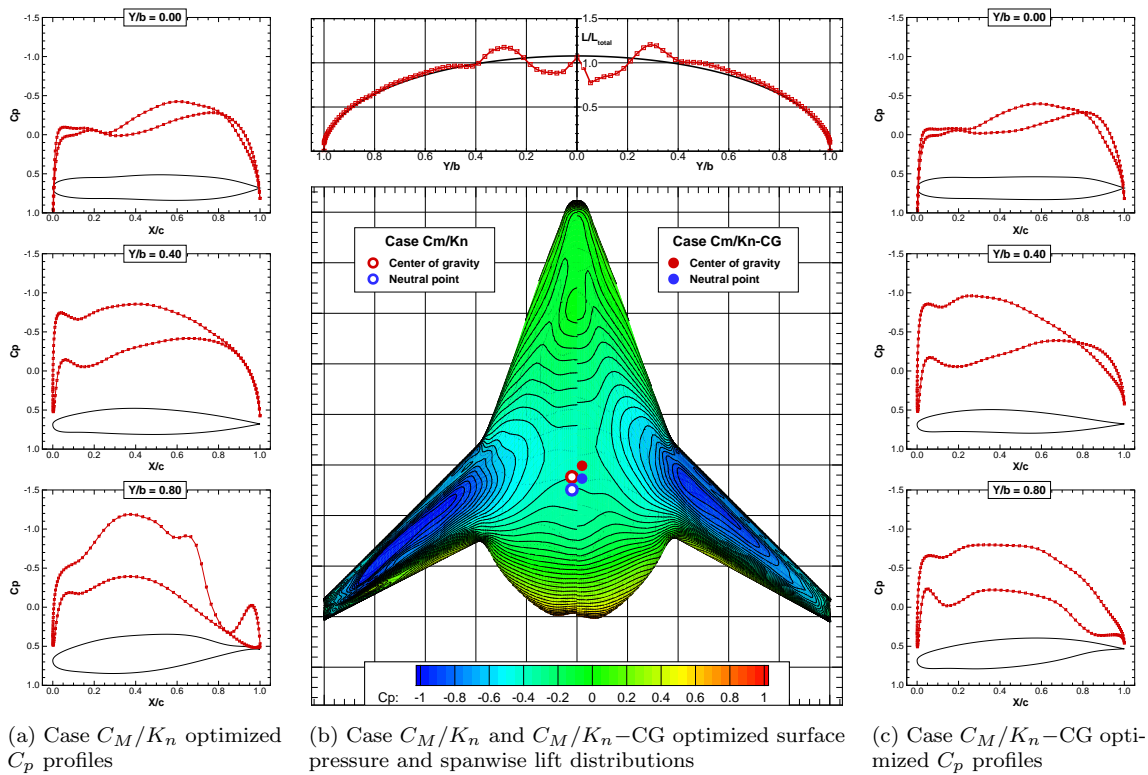


Figure 5: Inviscid pressure and spanwise lift distributions on the Case C_M/K_n and C_M/K_n -CG optimized designs.

both the pitching moment and static margin are constrained, the center of pressure and neutral point are also effectively defined. The optimizer has increased the sweep to the upper bound, and has therefore exhausted geometric means of moving the local aerodynamic centers aft to satisfy the static margin constraint. As a result, it must rely on section changes in order to properly locate the aerodynamic centers. On the outer portion of the wing, the optimizer chooses thick sections that rapidly decrease in thickness at approximately 80% chord. These sections lead to a fast pressure recovery at 80% chord, and at $y/b = 0.80$ a very localized shock develops, as shown in Figure 5a. These features result in the aft movement of the local aerodynamic centers. At 80% span the local aerodynamic center is at 26% chord for the Case C_M design, while it is moved to 30% chord in Case C_M/K_n . Since the planforms of Cases C_M and C_M/K_n are nearly identical, this movement of 4% chord is achieved primarily through section changes. Similar movement of the local aerodynamic centers occurs along the majority of the span. However, the sections used to obtain the required aerodynamic centers result in reduced performance at off-design conditions, as shall be demonstrated later.

Since the calculated CG location is relatively approximate, we introduced the perturbation, Δ_{CG} , as described previously, to arrive at Case C_M/K_n -CG, shown in the right half of Figure 5. Again, wave drag has been eliminated and the elliptical distribution is recovered on the wing. The contorted pressure profiles on the wing which were seen in Case C_M/K_n are absent. The optimizer has moved the Δ_{CG} variable ahead of the calculated point by 2% of the body length to a point which serves as a compromise between the trim and stability requirements. This allows the 5.5% drag penalty seen in Case C_M/K_n to be reduced to 2.0%. In Case C_M the optimizer finds fore-loaded sections in order to trim the aircraft while using very little reflex. While still using fore-loaded sections in Case C_M/K_n -CG, more reflex is seen, particularly on the inboard sections, such that the aft of the aircraft acts as the tail in a conventional design to trim and stabilize the aircraft.

Undesirable stability characteristics also emerge at off-design lift coefficients for Case C_M/K_n . Figure 6a shows the pitching moment behaviour of each design over a range of lift coefficients. As required, Cases C_M/K_n and C_M/K_n -CG have a negative $\frac{\partial C_M}{\partial C_L}$ at the design C_L . At lift coefficients other than this, Case C_M/K_n -CG maintains a relatively constant $\frac{\partial C_M}{\partial C_L}$ until nonlinear features – such as shocks – begin to emerge

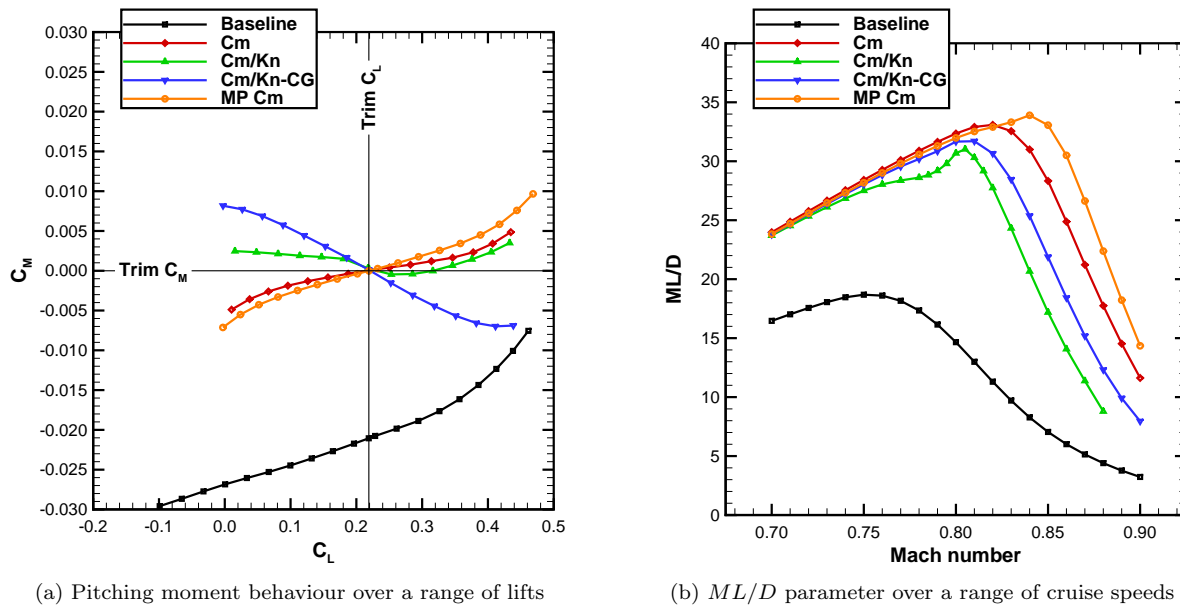


Figure 6: Inviscid performance of each design at off-design conditions.

Case	AoA	C_L	C_M	K_n	L/D
Baseline	3.78°	0.219	0.0070	-15.6%	10.3
Euler-optimized Case C_M	3.74°	0.219	0.0102	-5.5%	15.6

Table 5: Baseline and Euler-optimized geometries analyzed using RANS at the target lift.

at high and low angles-of-attack. In contrast, Case C_M/K_n only has the required $\frac{\partial C_M}{\partial C_L}$ in a very narrow band about the design point. This is due to the tailoring of the pressure profiles to attain the required aerodynamic centers at the design point and the resulting movement of the aerodynamic centers at off-design conditions.

Finally, the multipoint version of Case C_M described in Subsection B is presented. At the main design point (i.e. the center quadrature point), a 1.0% drag penalty is paid relative to the equivalent single-point case. The parameter ML/D from the Breguet range equation

$$\text{Range} = \frac{a}{c_T} \frac{ML}{D} \ln \left(\frac{W_{\text{initial}}}{W_{\text{final}}} \right) \quad (6)$$

where a is the speed of sound at cruise conditions, and c_T is the thrust specific fuel consumption, is shown for the baseline and each optimized design in Figure 6b. The multipoint optimization achieves a maximum ML/D which is 3.0% higher than the equivalent single-point case, and this maximum occurs at Mach 0.84 instead of 0.82. With the exception of Case C_M/K_n , which suffers from the reemergence of shocks at off-design speeds due to the thick wing sections (which exhibit localized shocks even at the design point, as discussed earlier), very little point optimization is seen. At the design point the penalty from the stability constraint is 2.0% for Case C_M/K_n -CG. However, comparing Cases C_M and C_M/K_n -CG in Figure 6b demonstrates that this penalty increases significantly at higher cruise speeds due to the fact that shocks emerge much sooner on the Case C_M/K_n -CG design than the Case C_M design.

B. Euler-Based Optimization Results Analyzed Using RANS

The Case C_M Euler-optimized shape presented in the previous section is now analyzed using the RANS equations at the target lift, with the performance shown in Table 5. Compared to the 55% drag reduction seen in the Euler solution, the drag reduction when analyzed with RANS is 34%. Figure 7 shows the pressure profiles of the Euler-optimized design obtained from the Euler and RANS solutions. As described previously

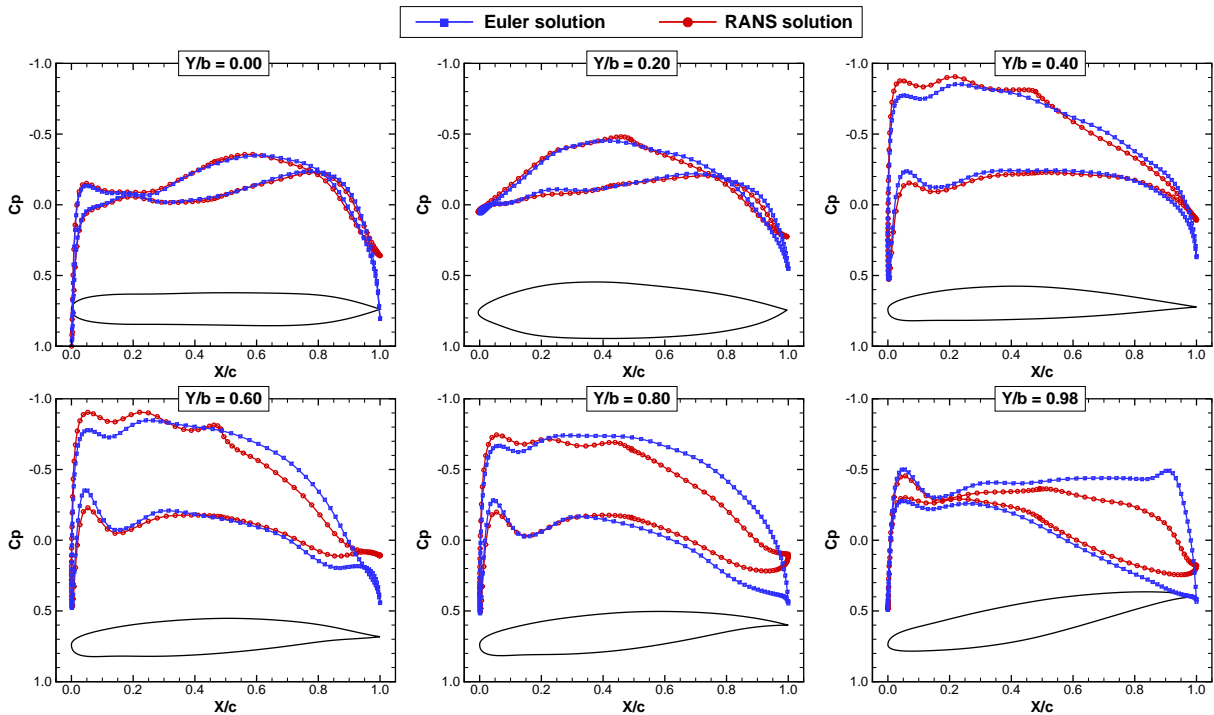


Figure 7: C_p profiles on the Euler-optimized Case C_M geometry for both the Euler and RANS solutions at the target lift.

Case	AoA	C_L	C_M	K_n	L/D
Baseline	3.78°	0.219	0.0070	-15.6%	10.3
C_M	2.98°	0.219	0.0003	-4.0%	16.7

Table 6: Summary of performance for the baseline and RANS-optimized case.

the Euler-optimization removes the shock, yet when this same design is analyzed with RANS a weak shock begins to reappear over a very small portion of the wing at 50% span. It is also interesting to note the different pressure distributions which are given by the Euler and RANS solutions. On the body the two solutions agree very well; however the outboard sections exhibit significant deviation. The sharp pressure recoveries at the trailing edge in the Euler solution cannot be maintained in a turbulent flow and this results in separation as evidenced by the flat portion of the pressure profile at the trailing edge from 60% span outward in the RANS solution. This separation is visualized in Figure 8b with stream traces extracted from the solution a short distance above the upper surface. While separation is still present on the Euler-optimized shape, its magnitude is greatly reduced compared to the baseline, thanks to the elimination of shock-boundary-layer interaction and the resulting separation. Finally, the inability to maintain the high aft loading in the RANS solution also decreases the local lift coefficient on the outboard sections and thus the elliptical distribution on the wing, which was achieved during the Euler optimization, is lost in the RANS solution, as seen in Figure 9.

C. RANS-Based Optimization Results

Finally, the results of the optimization using the RANS equations are shown in Table 6. The pressure distributions on the baseline and Case C_M designs are shown in Figure 10. As in the Euler case, the baseline spanwise lift distribution is non-elliptical and a shock is present on the wing. The neutral point is also very far forward. Figure 8a shows how shock-boundary-layer interaction on the wing induces significant separation and crossflow, while on the body a large recirculation region is seen at the trailing edge. Both

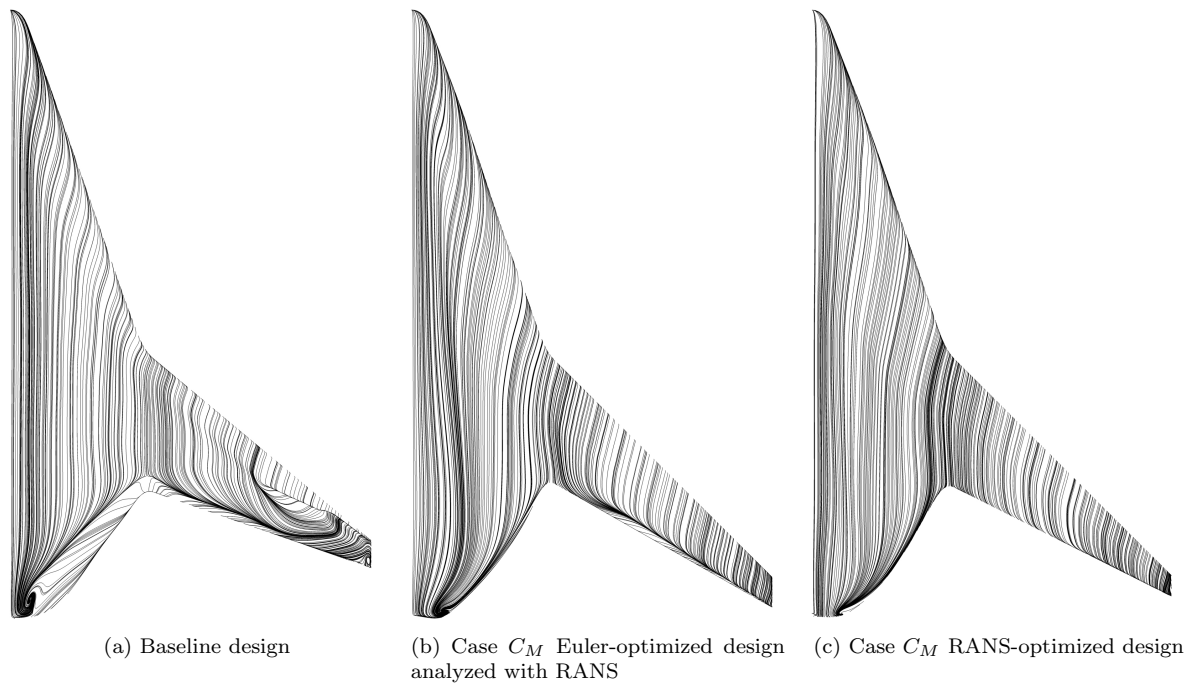


Figure 8: Stream traces for the RANS solutions on the baseline and Case C_M optimized designs.

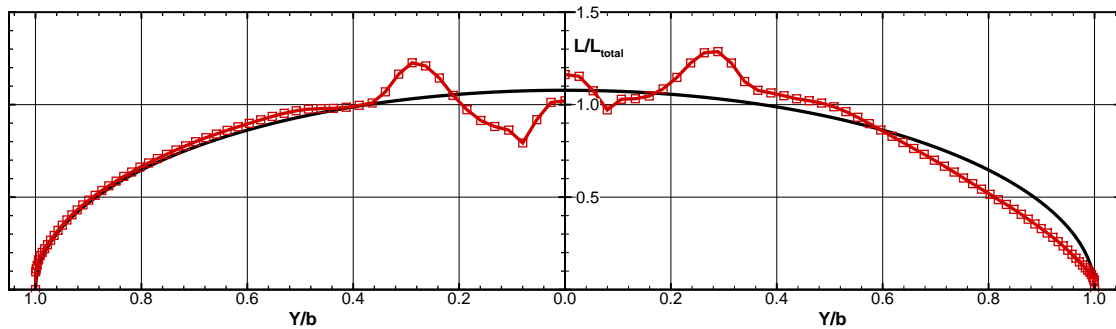


Figure 9: Spanwise lift distributions for the Euler-optimized Case C_M geometry analyzed using the Euler (left) and RANS (right) equations at the target lift.

of these features introduce significant pressure drag. The optimizer has eliminated the shocks and achieved an elliptical distribution on the wing while simultaneously trimming the design and increasing the static margin, although it is still negative. Significantly lower pressure gradients on the aft portion of the sections can be seen in Figure 10c compared to the baseline and the Euler-optimized Case C_M results. This leads to near-elimination of separated flow, and hence lower pressure drag. However, small recirculation regions are still present at the trailing edge of the body and outboard portion of the wing, as shown by the stream traces in Figure 8c. A drag reduction of 38% is achieved through RANS-based optimization. However the final L/D value is only 16.7, which is lower than a conventional regional jet. If the BWB is to be competitive it must achieve a higher L/D than an equivalent conventional design. This is the first application of RANS-based optimization to this problem, and it is anticipated that further study shall be able to reduce the drag further. In particular, elimination of the remaining regions of separated flow is expected to be possible.

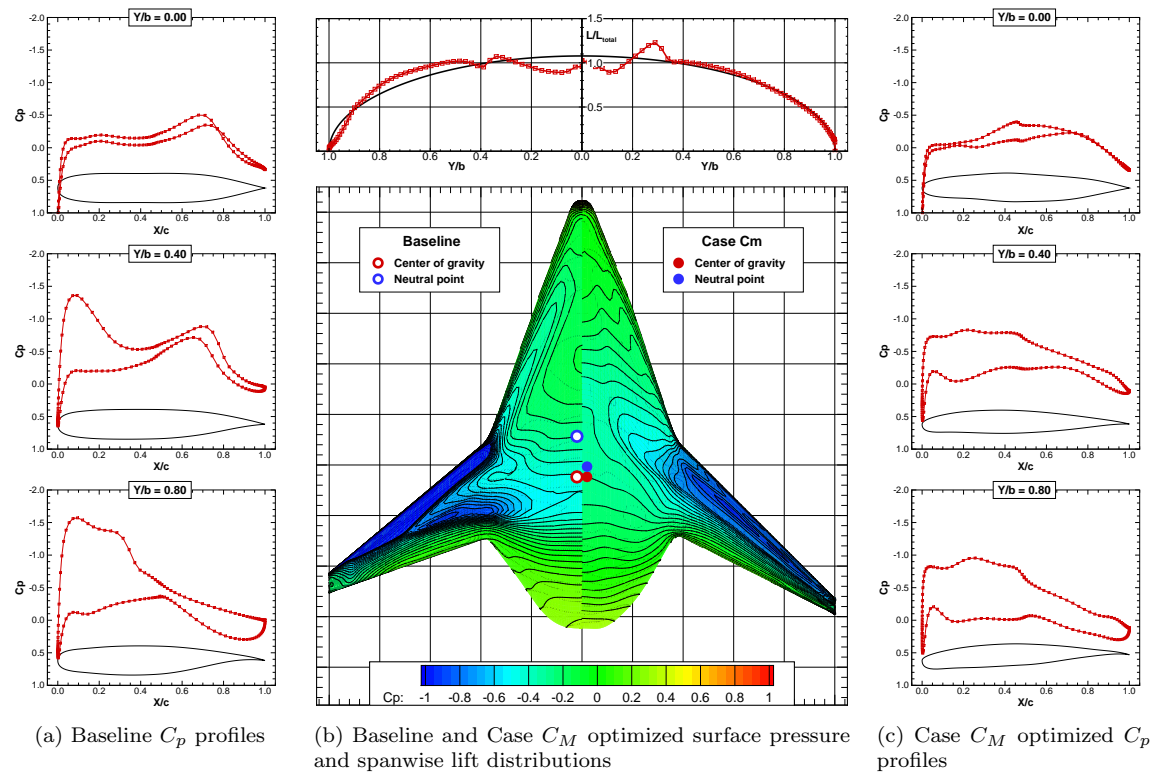


Figure 10: Pressure and spanwise lift distributions from the RANS solutions on the baseline and Case C_M RANS-optimized designs.

VI. Conclusions

Aerodynamic shape optimization has been applied to a regional class blended-wing-body aircraft. Using both the Euler and RANS equations, the baseline design was optimized subject to a variety of constraints; including trim and longitudinal static stability. Euler-based optimization yielded up to a 55% drag reduction, while RANS-based optimization yielded a 38% drag reduction. The imposition of a stability constraint incurs up to a 5% drag penalty and can lead to significant performance degradation at off-design conditions; however these penalties can be significantly reduced by small changes in the center of gravity location. Multipoint optimization was performed to optimize performance over a range of possible missions. Euler-based optimization eliminated the shocks on the baseline design and reduced the induced drag by achieving an elliptical load distribution on the wing. RANS-based optimization reduced the significant amount of pressure drag on the baseline design by nearly eliminating regions of separated flow, in addition to minimizing induced and wave drag. The lift-to-drag ratio of the RANS-optimized design falls short of that required if the BWB is to surpass conventional regional jet designs. However, this is a first attempt at RANS-based optimization for this geometry and mission, and with further study, higher aerodynamic efficiency should be attainable. Future work shall include the aerodynamic shape optimization of an equivalent conventional regional jet design such that a direct performance comparison can be made. In addition, aerostructural optimization tools are under development which shall be applied to this problem in order to find the aerostructural optimum.

Acknowledgments

The authors would like to acknowledge the financial support of Bombardier Aerospace, under the auspices of the Green Aviation Research and Development Network, the Natural Sciences and Engineering Research Council of Canada, and the University of Toronto. Computations were performed on the Parallel supercomputer at the WestGrid HPC Consortium. WestGrid is a member of Compute Canada.

References

- ¹Liebeck, R., "Design of the Blended Wing Body Subsonic Transport," *Journal of Aircraft*, Vol. 41, No. 1, 2004, pp. 10–25.
- ²Hileman, J. I., Spakovszky, Z. S., Drela, M., Sargeant, M. A., and Jones, A., "Airframe Design for Silent Fuel-Efficient Aircraft," *Journal of Aircraft*, Vol. 47, No. 3, 2010, pp. 956–969.
- ³Li, V. and Velicki, A., "Advanced PRSEUS Structural Concept Design and Optimization," *12th AIAA/ISSMO Multidisciplinary Analysis and Optimization Conference*, AIAA-2008-5840, Victoria, BC, September 2008.
- ⁴Mukhopadhyay, V., "Blended-Wing-Body Fuselage Structural Design for Weight Reduction," *46th Structures, Structural Dynamics and Materials Conference*, AIAA-2005-2349, Austin, TX, April 2005.
- ⁵Hansen, L. U., Heinze, W., and Horst, P., "Blended Wing Body Structures in Multidisciplinary Pre-Design," *Structural and Multidisciplinary Optimization*, Vol. 38, No. 1, 2008, pp. 93–106.
- ⁶Vicroy, D. D., "Blended-Wing-Body Low-Speed Flight Dynamics: Summary of Ground Tests and Sample Results," *47th AIAA Aerospace Sciences Meeting and Exhibit*, AIAA-2009-0933, Orlando, FL, January 2009.
- ⁷Voskuil, M., La Rocca, G., and Dircken, F., "Controllability of Blended Wing Body Aircraft," *26th International Congress of the Aeronautical Sciences*, Anchorage, AL, September 2008.
- ⁸Gern, F. H., "Improved Aerodynamic Analysis for Hybrid Wing Body Conceptual Design Optimization," *50th AIAA Aerospace Sciences Meeting and Exhibit*, AIAA-2012-0249, Nashville, TN, January 2012.
- ⁹Nickol, C. L., "Hybrid Wing Body Configuration Scaling Study," *50th AIAA Aerospace Sciences Meeting and Exhibit*, AIAA-2012-0337, Nashville, TN, January 2012.
- ¹⁰Wakayama, S., "Blended-Wing-Body Optimization Problem Setup," *8th AIAA/USAF/NASA/ISSMO Symposium on Multidisciplinary Analysis and Optimization*, AIAA-2000-4740, Long Beach, CA, September 2000.
- ¹¹Hileman, J. I., Spakovszky, Z. S., Drela, M., and Sargeant, M. A., "Airframe Design for "Silent Aircraft"," *45th AIAA Aerospace Sciences Meeting and Exhibit*, AIAA-2007-0453, Reno, NV, January 2007.
- ¹²Morris, A. J., "MOB: A European Distributed Multi-Disciplinary Design and Optimisation Project," *9th AIAA/ISSMO Symposium on Multidisciplinary Analysis and Optimization*, AIAA-2002-5444, Atlanta, GA, September 2002.
- ¹³Méheut, M., Grenon, R., Carrier, G., Defos, M., and Duffau, M., "Aerodynamic Design of Transonic Flying Wing Configurations," *CEAS Katnet II Conference on Key Aerodynamic Technologies*, Breme, Germany, May 2009.
- ¹⁴Peigin, S. and Epstein, B., "Computational Fluid Dynamics Driven Optimization of Blended Wing Body Aircraft," *AIAA Journal*, Vol. 44, No. 11, 2006, pp. 2736–2745.
- ¹⁵Qin, N., Vavalle, A., Le Moigne, A., Laban, M., Hackett, K., and Weinerfelt, P., "Aerodynamic Considerations of Blended Wing Body Aircraft," *Progress in Aerospace Sciences*, Vol. 40, No. 6, 2004, pp. 321–343.
- ¹⁶Le Moigne, A. and Qin, N., "Aerofoil Profile and Sweep Optimisation for a Blended Wing-Body Aircraft Using A Discrete Adjoint Method," *The Aeronautical Journal*, Vol. 110, No. 1111, 2006, pp. 589–604.
- ¹⁷Kuntawala, N. B., Hicken, J. E., and Zingg, D. W., "Preliminary Aerodynamic Shape Optimization Of A Blended-Wing-Body Aircraft Configuration," *49th AIAA Aerospace Sciences Meeting*, AIAA-2011-0642, Orlando, FL, January 2011.
- ¹⁸Hicken, J. E. and Zingg, D. W., "A Parallel Newton-Krylov Solver for the Euler Equations Discretized Using Simultaneous Approximation Terms," *AIAA Journal*, Vol. 46, No. 11, 2008, pp. 2773–2786.
- ¹⁹Osusky, M. and Zingg, D. W., "A Parallel Newton-Krylov-Schur Flow Solver for the Reynolds-Averaged Navier-Stokes Equations," *50th AIAA Aerospace Sciences Meeting and Exhibit*, AIAA-2012-0442, Nashville, TN, January 2012.
- ²⁰Hicken, J. E. and Zingg, D. W., "Aerodynamic Optimization Algorithm with Integrated Geometry Parameterization and Mesh Movement," *AIAA Journal*, Vol. 48, No. 2, 2010, pp. 401–413.
- ²¹Zingg, D. W., Nemec, M., and Pulliam, T. H., "A Comparative Evaluation of Genetic and Gradient-Based Algorithms Applied to Aerodynamic Optimization," *REMN*, Vol. 17, No. 1, 2008, pp. 103–126.
- ²²Chernukhin, O. and Zingg, D. W., "Multimodality and Global Optimization in Aerodynamic Design," *AIAA Journal*, Vol. 51, No. 6, 2013, pp. 1342–1354.
- ²³Gill, P. E., Murray, W., and Saunders, M. A., "SNOPT: An SQP Algorithm for Large-Scale Constrained Optimization," *Society for Industrial Applied Mathematics Review*, Vol. 47, No. 1, 2005, pp. 99–131.
- ²⁴Hicken, J. E. and Zingg, D. W., "Induced Drag Minimization of Nonplanar Geometries Based on the Euler Equations," *AIAA Journal*, Vol. 48, No. 11, 2010, pp. 2564–2575.
- ²⁵Osusky, L. and Zingg, D. W., "A Novel Aerodynamic Shape Optimization Approach for Three-Dimensional Turbulent Flows," *50th AIAA Aerospace Sciences Meeting and Exhibit*, AIAA-2012-0058, Nashville, TN, January 2012.
- ²⁶Bradley, K. R., "A Sizing Methodology for the Conceptual Design of Blended-Wing-Body Transports," Tech. Rep. NASA/CR-2004-213016, NASA/Langley Research Center: Joint Institute for Advancement of Flight Sciences, 2004.
- ²⁷Roskam, J., *Airplane Design Part V: Component Weight Estimation*, Aviation and Engineering Corporation, 1989.
- ²⁸Mozdzanowska, A. and Hansman, R. J., "Evaluation of Regional Jet Operating Patterns in the Continental United States," Tech. Rep. ICAT-2004-1, International Center for Air Transportation, 2004.
- ²⁹Martínez-Val, R., Pérez, E., Alfaro, P., and Pérez, J., "Conceptual Design of a Medium Size Flying Wing," *Journal of Aerospace Engineering*, Vol. 221, No. 1, 2007, pp. 57–66.
- ³⁰Buckley, H. P. and Zingg, D. W., "An Approach to Aerodynamic Design Through Numerical Optimization," *AIAA Journal*, in press, 2013.